Improving the Prediction of Soot Emissions and Contrail Formation from Modern Turbofans Using Alternative Fuels

Mafalda Narciso
mafalda.narciso@tecnico.ulisboa.pt

Instituto Superior Técnico, Universidade de Lisboa, Portugal

July 2021

Abstract

Condensation trails and contrail cirrus are currently responsible for the largest contribution to radiative forcing in the aviation sector, yet they have lifetimes of only a few hours. Their much shorter lifetimes when compared to long-lived greenhouse gases makes them ideal for the implementation of short-term mitigation measures. The use of Sustainable Aviation Fuel (SAF) instead of regular jet fuel has been associated to a reduction in soot particle emissions, leading to a decrease in initial ice crystal numbers in contrails, but also to a possible increase in contrail frequency and contrail ice mass due to higher water vapor emissions. A computational model was used to explore the influence of the variations of soot and water vapor emissions when using SAF and SAF blends in the formation of contrails, their ensuing optical depth, and their lifespan. An increase in frequency of contrails was found in cases where regular jet fuel emissions were close to threshold conditions. Reductions in contrail lifetime of up to 76% were found for contrails with lifetimes of over 30 minutes, while decreases in optical depth of up to 37% were found for contrails formed in air with a relative humidity of 42% or more. This work provides a better understanding of the potential of SAF as a mitigation measure against the impact of contrails on global warming.
Keywords: contrail, contrail cirrus, sustainable aviation fuel, soot, particle emissions, radiative forcing

1. Introduction

In 2017, a report [1] was published presenting the data obtained in several test-flights which used a 50:50 blend of low-sulfur Jet A fuel and a Camelina-based HEFA biojet fuel (HEFA C.). During the test-flights it was found that soot particle emissions could be up to over 50 % lower for the HEFA C. blend when compared to a Jet A fuel with medium sulfur content. This reduction in soot emissions was connected to a marked reduction in the formation of condensation trails, despite the higher water vapour emissions when burning the blend.

At the time of the report, the aviaton sector contributed approximately 5 % of the global anthropogenic Radiative Forcing (RF), with the RF attributed to contrails and contrail cirrus being estimated as 50 mWm^{-2}, making it the largest contribution in the sector. Yet, contrail cirrus have a much shorter lifetime than long-lived greenhouse gases; this influences their relative importance when it comes to estimating the long-term climatic impact of the aviation sector [2], and also makes them very suitable for mitigation efforts since the effects would become very quickly apparent [3].

This work seeks to investigate the influence of Sustainable Aviation Fuel (SAF) on contrail formation and contrail cirrus properties, taking into account the effect of the differences in soot emissions, water vapour emissions, and other combustion and exhaust properties.

2. Contrails and Contrail Cirrus

Cirrus clouds are ice clouds found in the upper troposphere in areas where the temperature is below approximately −40 °C; above this temperature mixed-phase clouds, clouds with both liquid water droplets and ice crystals, are typically found. Cirrus clouds reflect shortwave solar radiation and trap long-wave thermal radiation, having a large effect on the global RF due to their persistence at high altitudes if the temperature is low enough. On average, their effect is to heat the Earth's atmosphere.

Cirrus clouds require a Relative Humidity (RH) over ice of over 145 %, classified as high ice supersaturation, to form, and ice saturation to persist. The reason behind this disparity is that newly formed ice crystals are not in equilibrium with the

ice supersaturated air around them. Cirrus clouds are set apart from other clouds in both formation and persistence requirements, seeing as other clouds form and evaporate at temperatures slightly above and below liquid water saturation [4][5].

Contrary to cirrus clouds, contrail cirrus only require the environment to be at ice saturation. During a flight, the aircraft engine releases both water vapour and heat; the former promotes water saturation while the latter hinders it. The heat release leads to an increase in temperature which in turn leads to an increase in the vapour concentration required for saturation. For contrails to form, the water vapour concentration increase due the emitted water vapour has to be greater than the increase in local plume liquid water saturation point due to the emitted heat. These plume conditions can be achieved without the high ice supersaturation environment required for cirrus cloud formation, requiring only an environment at ice saturation.

When mixed with sufficiently dry ambient air, contrails evaporate soon after their formation and are classified as short-lived contrails. Yet, their conditions for evaporation are the same as those for cirrus clouds, meaning that in an ice supersaturated environment they can be formed and persist until either the RH drops below ice saturation or they sediment into drier air [6].

This means that in a substantial fraction of the upper troposphere, contrail cirrus can form and persist in air that is cloud free, increasing the high cloud coverage in environments where cirrus clouds would not be able to form.

3. Implementation

A model based on the Contrail Cirrus Prediction Tool (CoCiP) developed by U. Schumann [7] is implemented using atmospheric data from the ERA-20CM model ensemble for the year 2010 [8]. The ensemble gives the mean monthly values for a set of local atmospheric parameters at different latitudes, longitudes and pressure levels; this allows the atmosphere to be modelled in 3D space.

An aircraft with characteristics similar to the BAe 146 was used for the simulations, and an engine model created by R. Gaspar [9] was employed here to distinguish between the different SAF. This was coupled with the Rizk and Mongia model [10] for the prediction of soot emissions of the different fuels.

3.1. Contrail Model

The contrail model is divided into sections due to the different approaches employed in the simulation of the different parts of the contrail life. The Schmidt-Appleman Criterion (SAC) is used to ascertain whether there is formation of contrails for local conditions, a parametric model is used to treat the vortex phase, and throughout the rest of the contrail lifetime a second order Runge-Kutta scheme is used to simulate advection, with contrail properties being calculated at each step.

3.1.1 Contrail Formation

The thermodynamic formation of contrails is explained using the SAC, which asserts that for contrail formation to occur, liquid saturation has to occur locally in the plume of exhaust gases during mixing with the cold ambient air. This condition is satisfied when the ambient temperature is below a certain threshold temperature, T_C.

The amount of water vapour in the exhaust is one of the key factors in the formation of contrails. For every unit mass of fuel, there will be EI_{H_2O} mass units of water vapour emitted. The water vapour emission index, EI_{H_2O}, is obtained with equation 1, which is dependent on the molar masses of hydrogen and water, M_{H_2O} and M_H, and on the hydrogen mass ratio in the fuel, m_H [6].

$$EI_{H_2O} = \frac{m_H M_{H_2O}}{2M_H} \tag{1}$$

The heat in the exhaust gases is another key factor for the formation of contrails. When burning the fuel with air, the engine will release a combustion heat Q per unit mass of fuel. A fraction η of the combustion heat will be converted into work to propel the aircraft, while the rest, $(1-\eta)Q$ per unit mass of fuel, will be released with the exhaust gases. This fraction η is the overall overall propulsion efficiency of the aircraft and is calculated with equation 2, where F is the thrust, TAS is the true airspeed of the aircraft, Q is the fuel combustion heat and $\dot{m}_F$ is the fuel flow rate [6].

$$\eta = \frac{F \times TAS}{Q\dot{m}_F} \tag{2}$$

In an $e - T$ plot the saturation pressures over liquid water, e_L, and ice, e_I, remain invariant under changes in air pressure, and therefore altitude. In this case, only the steepness of the mixing line, G, varies. Assuming constant c_p, the steepness of the mixing line can be computed from:

$$G = \frac{R_{H_2O}}{R_{air}} \frac{c_p EI_{H_2O} P}{Q(1-\eta)} \tag{3}$$

Since the gradient G of the mixing line is constant, the threshold temperature, T_C, follows by Newton iteration, along with T_M, from equation 4. In this equation, $e_{sat}(T_C)$ is the vapour pressure in the environment under threshold conditions, U_{amb} is the ambient RH over water, and T_M is the temperature at the point where the plume mixing line

in an $e - T$ plot touches the liquid saturation curve [6].

$$T_C = T_M - \frac{e_{sat}(T_M) - U_{amb} e_{sat}(T_C)}{G} \quad (4)$$

3.1.2 Wake Vortex Phase

The mass mixing ratio of ice in the contrail at the time of its formation, I_0, is obtained from equation 5 as a function of the water mass emitted by the engines per flight distance, the ambient humidity, q_0, and the saturation humidity, $q_{sat}(P_0, T_0)$ at the engine exit.

$$I_0 = \frac{EI_{H_2O} m_F}{\frac{\pi}{4} \rho D_1 B_1} + q_0 - q_{sat}(P_0, T_0) \quad (5)$$

The initial number of ice particles, $N_{i,0}$, is obtained from the number of soot particles which were emitted during combustion per kg-fuel, EI_N, as seen in equation 6. While in principle volatile aerosols can also become nucleus for the ice particles, their contribution is relatively small for typical soot emissions and moderately low temperatures.

$$N_i = \frac{EI_N m_F}{TAS} \quad (6)$$

The details of the complex jet and wake dynamics in the first few minutes of the contrail lifetime are not resolved, instead the properties of the contrail at the end of the wake vortex phase are estimated as a function of aircraft and atmospheric parameters.

Young contrails interact with the engine jet, the aircraft wake vortex, and with ambient turbulence, stratification and wind shear; the details of this interaction are aircraft dependent. The parametric model [7] employed here accounts for aircraft wingspan and mass, True Air Speed (TAS), and local air density, Brunt-Väisälä frequency and Eddy Dissipation Rate (EDR).

3.1.3 Contrail Trajectory and Properties

The location of the contrail is set in three-dimensional space to account for the variation with longitude and latitude of the environmental parameters it requires in its calculations. For the horizontal trajectory the position is given according to its longitude, x, and latitude, y, while for the vertical trajectory the position is given according to the ambient pressure, P.

To calculate the trajectory the model uses the standard second-order two-step Runge-Kutta scheme. The time derivatives for each position are given by equations 7a, 7b and 7c. For the latitude and longitude time derivatives, U represents the eastward wind in m/s and V represents the northward wind in m/s. For the vertical time derivative, ω represents the vertical pressure change rate in Pa/s and is obtained from the atmospheric data ensembles.

$$\frac{\partial x}{\partial t} = U \quad (7a)$$

$$\frac{\partial y}{\partial t} = V \quad (7b)$$

$$\frac{\partial P}{\partial t} = \omega + \rho_{air} g V_T \quad (7c)$$

The ice crystal terminal fall velocity is computed using equation 8, where μ_{air} is the air dynamic viscosity, D_{ice} is the maximum dimension of an ice crystal and Re is the Reynolds number [11].

$$V_T = Re \frac{\mu_{air}}{D_{ice} \rho_{air}} \quad (8)$$

The maximum dimension of a crystal, D_{ice}, varies with temperature and crystal shape. It was obtained from measurements made in ice clouds which were made available for pristine columns, plates, and component bullets of bullet rosettes [12].

The effective cross-sectional area of the contrail is obtained from an integral over y and z, as seen in equation 9, where $\sigma(\mathbf{x}, t)$ is the covariance matrix of the concentration field $\mathbf{x}$ as seen in equation 10, where c(x) is the concentration of a species per air mass in the plane perpendicular to the contrail axis.

$$A = \int\int exp(-\frac{1}{2} \mathbf{x}^T \sigma^{-1} \mathbf{x}) d\mathbf{x} = 2\pi (det(\sigma))^{\frac{1}{2}} \quad (9)$$

$$\sigma = \int\int (\mathbf{x} \otimes \mathbf{x}) c(\mathbf{x}) d\mathbf{x} \quad (10)$$

The components of the covariance matrix describe a real symmetric and positive definite matrix, with a determinant as given in equation 11b. They are calculated for each time step as a function of shear, and the horizontal, vertical and shear diffusitivies, as seen in reference [7].

$$\sigma = \begin{pmatrix} \sigma_{yy} & \sigma_{yz} \\ \sigma_{yz} & \sigma_{zz} \end{pmatrix} \quad (11a)$$

$$det(\sigma) = \sigma_{yy} \sigma_{zz} - \sigma_{yz}^2 \quad (11b)$$

The width and the depth of the contrail for each time-step are obtained from the covariance matrix components as shown in equations 12a and 12b.

$$B = \sqrt{8 \sigma_{yy}} \quad (12a)$$

$$D = \sqrt{8 \sigma_{zz}} \quad (12b)$$

The product of the optical depth by the contrail width controls the radiative forcing of the contrail,

and it is a function of the area and the extinction, which can be computed as seen in reference [7] from the ice mass ratio and the ice particle number concentration per volume, $n = \frac{N_i}{A}$.

$$B\tau = \beta \int\int exp\left(-\frac{1}{2}\mathbf{x}^T\sigma^{-1}\mathbf{x}\right) dzdy = \beta A \quad (13)$$

When the optical depth, τ, reaches a small enough value, $\tau < 10^{-4}$, the simulation ends.

During the lifetime of the contrail, the water mass in the plume will mix with the ambient air humidity, changing its ice content. The humidity inside the plume is considered to be at ice saturation, $q_P = q_{sat}$. The mass mixing ratio of ice in the contrail for each time step is computed from equation 14, where q_E is taken as the mean value between the times t and $(t + \Delta t)$.

$$I(t+\Delta t) = \frac{M_{air}(t)(I(t)+q_{sat}(t)) + \Delta M_{air} q_E}{M_{air}(t+\Delta t)} - q_{sat}(t+\Delta t) \quad (14)$$

A particle loss model is implemented to account for changes in the particle number; it is represented in equation 15.

$$\left(\frac{dN_i}{dt}\right)_{loss} = \left(\frac{dN_i}{dt}\right)_{turb} + \left(\frac{dN_i}{dt}\right)_{agg} \quad (15)$$

Two sources for particle loss are considered. The first is the plume-internal turbulence, that is, the sublimation of smaller particles during the turbulent mixing of the contrails with dry ambient air. The second is the sedimentation-induced aggregation, that is, the process in which large falling ice particles collide and aggregate with smaller ice particles, decreasing in this way the particle number.

The turbulence losses, as shown in equation 16a, are a function of the vertical and horizontal diffusivities, D_V and D_H, and the contrail's depth, width and effective depth, $D_{eff} = \frac{A}{B}$. The aggregation losses, as shown in equation 16b, are a function of the particle terminal fall velocity, the ice particle number concentration per volume, and a mean volume particle radius, r_P, which depends on the ice mass and the ice particle number of the contrail.

$$\left(\frac{dN_i}{dt}\right)_{turb} = \left(\frac{D_H}{max(B,D)^2} + \frac{D_V}{D_{eff}^2}\right) N_i \quad (16a)$$

$$\left(\frac{dN_i}{dt}\right)_{agg} = 8\pi {r_p}^2 V_T n N_i \quad (16b)$$

3.2. Soot model

The Rizk model [10] is an empirical model used for the calculation of soot mass emissions which takes into account the soot formation and the soot oxidation. It is expressed according to equation 17. In this model the formation is associated with the primary zone and the oxidation is associated with the secondary zone, but the model itself is 0-D and calculated in a single step.

$$EI_{soot} = 0.0145 \frac{f_{pz} P_{03}^2}{f\dot{m}_3 T_{pz}} (18 - H\%)^{1.5} \times \left(1 - 0.00515 \frac{exp(0.001 T_{sz})}{f_{sz}}\right) \quad (17)$$

The soot mass emissions are then converted to particle emissions using a mean radius for the primary particles, which are considered to be spherical.

Current understanding of soot formation dynamics establishes that particle number variation is not proportional to particle mass variation; soot particle radius increases with an increase in engine power, and shows marked differences depending on the fuel used. In particular, SAF blends with lower aromatics than typical Jet A-1 fuel have been shown to produce soot particles with a smaller mean radius [13].

Not enough data is available to establish a correlation between a fuel's composition and engine power and the aggregate and primary particle sizes ensuing from the combustion, so a mean radius is established for all fuels based on typical Jet A emissions. This could potentially lead to an underestimation of SAF soot particle emissions.

3.3. Validation

The engine has been extensively documented and validated previously, and for this implementation only suffered minor alterations with the objective of reducing its computation time which did not alter the results obtained with it. The validation for the model can thus be found in reference [9].

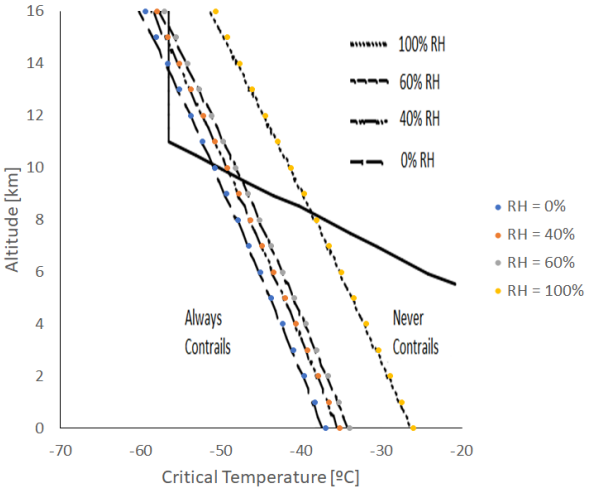

Figure 1: Threshold temperatures computed for 0 %, 40 %, 60 % and 100 % RH with engine and fuel parameters $\eta = 0.3$, $EI_{H_2O} = 1.223$ and $Q = 43$ MJ/kg. Comparison is done with adapted plot from reference [14].

Figure 1 shows a comparison between the threshold temperatures obtained in this study using the SAC with those expected. In this figure, the continuous thick line is the temperature profile of the International Standard Atmosphere (ISA).

Table 1 shows the comparison between computed and measured values for an aircraft with dimensions equivalent to a A319-111, flying at $TAS = 224$ m/s on flight level $FL = 320$ hft. This was one of the aircraft for which measurements were made in reference [15], and it was chosen since its dimensions were the closest to what an aircraft with the engine modeled in this work would have.

	Measured	Predicted	Error [%]
T [K]	217	216.62	0.18 %
N_{BV} [/s]	0.017	0.011	35.29 %
$\epsilon*$ [m^2/s^3]	4.75x10^{-6}	4.805x10^{-6}	-1.16 %
b_0 [m]	26.8	26.78	0.075 %
t_0 [s]	22.7	22.49	0.93 %
Δz_{max} [m]	120	143.29	-19.41 %

Table 1: Comparison of predicted and measured values for an aircraft with $M_a = 47000$ kg, $s_a = 34.1$ m, flying at $TAS = 224$ m/s at an altitude of 320 hft.

The largest difference comes from the computed Brunt-Väisälä frequency, which shows an error of 35.29 %. This can be shown to be responsible for the –19.41 % error in the maximum displacement value; if the Brunt-Väisälä frequency is set to $N_{BV} = 0.017$, the value obtained is $\Delta z_{max} = 120.5992$ m, with an error of only –0.05 %. Nevertheless, a difference of 20 or even 30 meters between the measured and computed values was expected and is still acceptable.

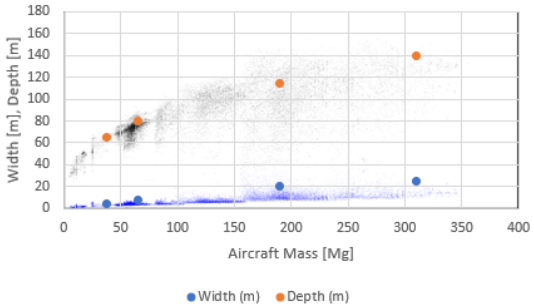

Figure 2: Depth and width at point 1 computed for BAe 146 ($s_a = 34.1$ m, $M_a = 38.1$ Mg) and example large, medium and small aircrafts with parameters obtained from reference [7], juxtaposed over plot where each point represents an aircraft flying over the North Atlantic during 6-9 June 2006.

Figure 2 represents the predicted values for the initial contrail dimensions at point 1 for different aircraft. The smallest example aircraft has the same dimensions as the BAe 146, the aircraft used for the simulations in this work, and the remaining aircraft are example aircraft of the types B747, A330 and B737, with aircraft mass, wing span, flight speed and fuel flow taken from reference [7]. The predicted values show an overall good agreement with the observed trend, with the largest deviation from the mean being for the initial width of the example large aircraft, with it nevertheless remaining within the expected values.

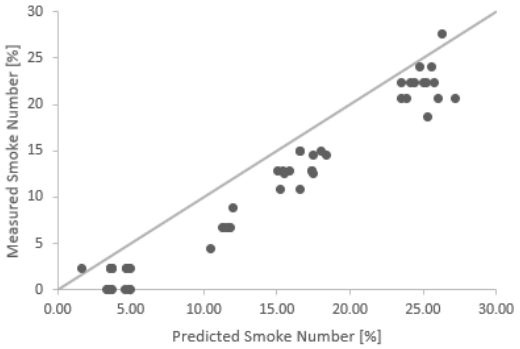

Figure 3: Rizk Model [10].

Figures 3 shows the correlation between the smoke number measured for the Lycoming ALF 502 [16] and the smoke number predicted with the Rizk and Mongia [10] model for similar conditions. The Rizk and Mongia model [10] tends to slightly overpredict the smoke number, but still shows an acceptable correlation.

Setting	Engine	Measured	Rizk Model
High	1	-23.67 %	-36.51 %
	2	-21.60 %	
Medium	1	-34.81 %	-36.66 %
	2	-44.49 %	
Low	1	-43.95 %	-36.85 %
	2	-55.14 %	

Table 2: Measured Relative Differences (RDs) in particle emissions from flight-tests [1] between a 50:50 HEFA C. blend and a medium-sulfur Jet A fuel, and RDs predicted with the Rizk Model [10] and the GSP Model [17] for the same fuels.

Table 2 compares the RDs in particle emissions obtained with the Rizk and Mongia [10] model with those measured in flight-tests; the comparison is done between a 50:50 blend of HEFA C. and a low-sulfur Jet A fuel, and a medium-sulfur Jet A fuel. The aircraft had four wing-mounted engines, with the exhaust plumes of the two inboard engines being measured; the data from both engines is presented, marked as Engine 1 and Engine 2.

The data is presented in relation to the thrust settings of the engine. It can be seen that measured data showed smaller RDs for high thrust settings, and higher RDs for low thrust settings. The model seems almost insensitive to this variation.

The model accounts for variations in fuel flow, and the particle emissions vary significantly for the different thrust settings, yet the RDs between blend

emissions and Jet A-1 emissions that show little variation. This lack of sensitivity could be attributed to the use of a mean radius which does not vary with thrust settings. Since the simulations are all carried out for average medium-thrust cruise conditions, this is not critical, but it is still worthy of note.

4. Results & discussion

4.1. SAF emissions

This section presents, for different pure SAF in relation to Jet A-1, the RD in the engine emissions and fuel properties which hold the most influence over the contrail model. Figures 4 and 5 show the RDs in water vapour emissions and in the net heat of combustion, respectively.

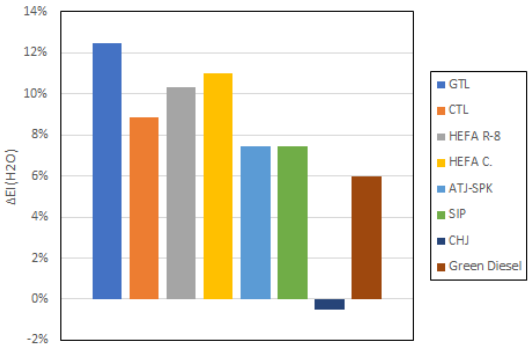

Figure 4: RDs in water vapour emissions between SAF and Jet A-1 fuel.

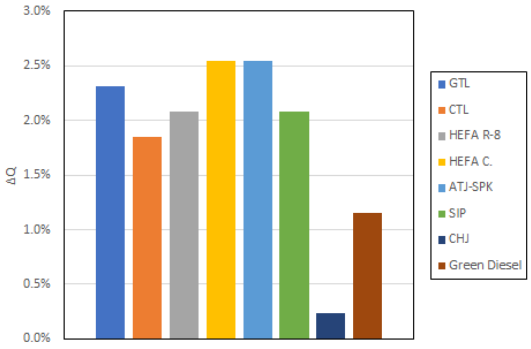

Figure 5: RDs in neat heat of combustion between SAF and Jet A-1 fuel.

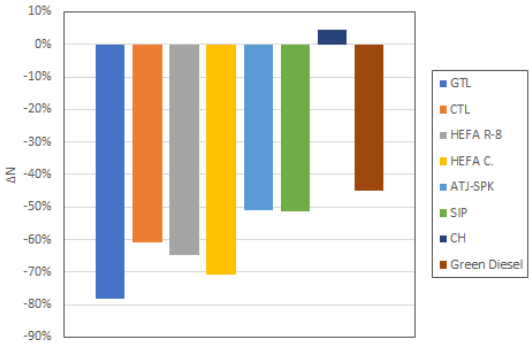

Figure 6: RDs in particle number emissions between SAF and Jet A-1 fuel.

Figure 6 shows the RDs in particle number emissions between each SAF and the Jet A-1 fuel for average cruise conditions. The propulsive efficiency of the aircraft also experienced minor variations ($<$1 %) when different fuels were burnt, but these did not seem to be great enough to influence the contrail formation frequency results.

4.2. Formation Frequency

An increase in contrail formation frequency was identified right behind and after Jet A-1 contrail formation areas; that is to say, in flight segments where contrails formed for all fuels, contrails were formed for most SAF slightly earlier (with contrails forming for CHJ slightly later).

There were no contrails formed for SAF outside of these conditions. In routes where contrails were not formed for Jet A-1, they were also not formed for the other fuels, and there were no isolated segments of contrails formed for SAF only. In other words, this increase in contrail formation frequency resulted in slightly longer contrails, and not in new separate contrails.

This results in an increase in frequency of under 1 % for the different fuels. This is better represented by the differences in the contrail formation threshold temperature.

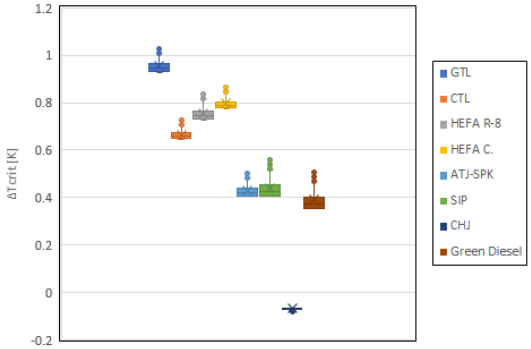

Figure 7: Absolute differences in threshold temperature between SAF and Jet A-1 fuel.

Figure 7 represents the absolute differences in threshold temperature between pure SAF and Jet A-1 fuel. As stated in section 3, contrails form when the ambient temperature is below the calculated threshold temperature for that location. As can be seen from the plots, the contrails for the different SAF will form at temperatures of $\sim$1 K or less from each other. While it is not impossible for isolated segments of SAF contrails to exist, the small difference in temperature explains why the frequency increase resulted only in longer contrails; it is unlikely for aircraft to reach SAF threshold temperatures without crossing to a degree under.

While the RDs in water vapour emissions control the general trend here, it can be seen that the RDs in the net heat of combustion of the fuels do hold an

observable influence over the formation frequency; despite the similar water vapour emission indices of SIP and ATJ-SPK, SIP has a lower net heat of combustion which results in slightly higher threshold temperatures.

4.3. Contrail lifetime

The main fuel-dependent factors influencing contrail properties are the water vapour emissions and the particle number emissions. All fuels show the same trend - an increase in water vapour emissions and decrease in particle number emissions - except for CHJ. To avoid redundancy, when SAF behaviour is described in this section it will be referring to all SAF with the exception of CHJ, with the implication that CHJ is displaying the opposite behaviour.

The contrail lifetime analysis is split into three parts due to the large deviation in values found between these: contrails with lifetimes of up to 30 minutes, contrails with lifetimes ranging from 30 minutes to 2 hours, and contrails with lifetimes greater than 2 hours.

Most contrails with lifetimes of 30 minutes or less have RDs in lifetime close to 0 %, but the Mean Relative Differences (MRDs) are dragged up due to the very high outliers. These outliers were all present in the same short segment, and seem to be the result of SAF contrails reaching higher RH areas shortly after the reference contrail lost its Ice Water Content (IWC).

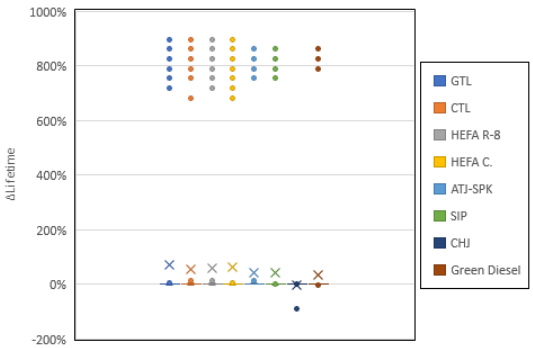

Figure 8: RDs in lifetime for reference contrails aged 30 minutes or less between SAF and Jet A-1 fuel.

At around the 20 minute mark, the lifetime of SAF contrails starts decreasing instead of increasing in relation to that of the reference contrails; this transition zone differs between the different fuels. Small decreases for SAF contrail lifetime were found as early as 14 minutes for GTL and HEFA C., at around 23 minutes for HEFA R-8, SIP and Green Diesel, and at around 27 minutes for CTL and ATJ-SPK.

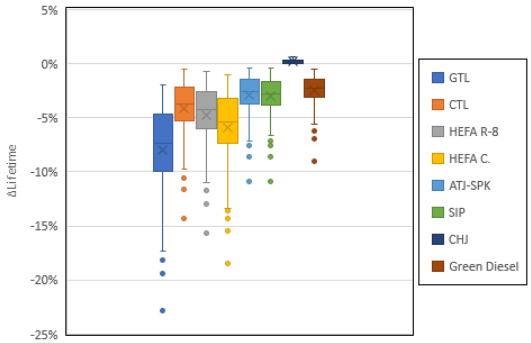

Figure 9: RDs in lifetime for reference contrails with lifetimes ranging from 30 minutes to 2 hours between SAF and Jet A-1 fuel.

It is important to note that while the RDs pale in comparison to those found for the previous time range, absolute differences are not that far apart. The outliers in figure 8, with increases of over 800 %, correspond to absolute differences of a bit less than 4 minutes, while mean values for this range correspond to absolute differences of around 5 minutes for GTL.

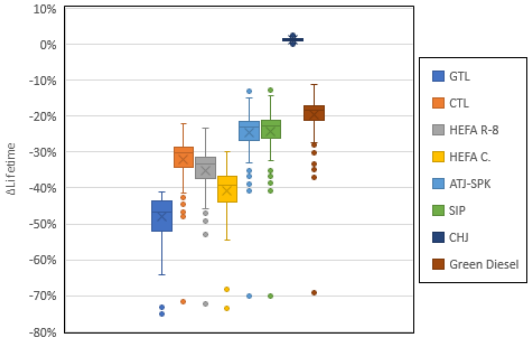

Figure 10: RDs in lifetime for reference contrails with lifetimes of over 2 hours between SAF and Jet A-1 fuel.

Figure 10 shows the RDs in lifetimes for reference contrails with lifetimes of over 2 hours, with the oldest contrails having lifetimes of a bit over 11 hours. This range represents the typical contrail cirrus lifetime, and, much like the previous range, shows a trend of sharper decreases for higher reference lifetimes.

4.4. Optical Depth

The optical depths immediately after the wake vortex are analysed first. These are the peak optical depths values for these contrails, found at typical lifetimes of less than a minute. Figure 11 shows the bulk of results; these were optical depths for contrails formed in environments with a RH of 43 % or higher.

The optical depths found in this range had typical values of 0.1 - 0.5, and the RDs between fuels seem to be mostly influenced by the particle emissions. The outliers plotted all correspond to contrails formed at RHs lower than 50 %. Contrails formed at these RHs tended to have higher

initial ice mass fractions, typically in the order of 10^{-5}, with smaller RDs between fuels.

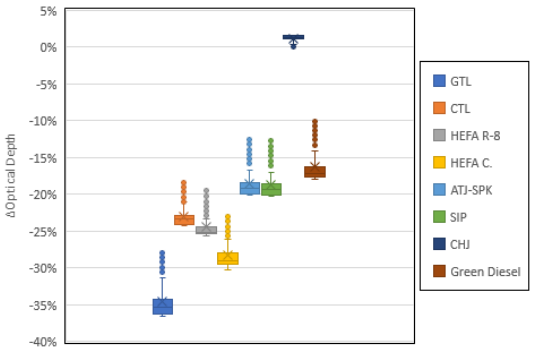

Figure 11: RDs in peak optical depths for ambient RHs at formation of 43 % or higher between SAF and Jet A-1 fuel.

Figure 13 shows the RDs for contrails formed at RHs of 41 % to 43 %. Contrails formed in these conditions had peak optical depths in the range of 0.02 - 0.1. Optical depths in this range are not visible in satellite observations and should have limited climatic impact.

The different SAF started yielding positive RDs at different RHs; GTL at a RH of ∼42 %, HEFA C. at ∼42.5 %, CTL and HEFA R-8 ∼42.7 % and the other fuels at around ∼43 %; the latter group includes CHJ, which started yielding negative RDs instead of positive RDs.

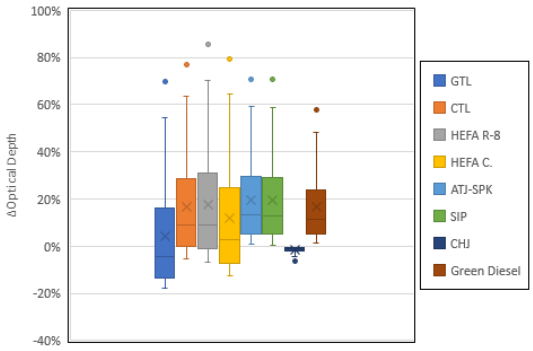

Figure 12: RDs in peak optical depths for ambient RHs at formation in the range of 41 % to 43 % between SAF and Jet A-1 fuel.

Contrails formed at RHs of 40 % or less fully lost their ice content during the wake vortex phase, and so optical depths for them were not calculated. A few contrails were formed or the RH range of 40 % to 41 %. Jet A-1 contrails formed in this range had optical depths of 0.0003 - 0.02, while SAF optical depths reached peak values of ∼0.04.

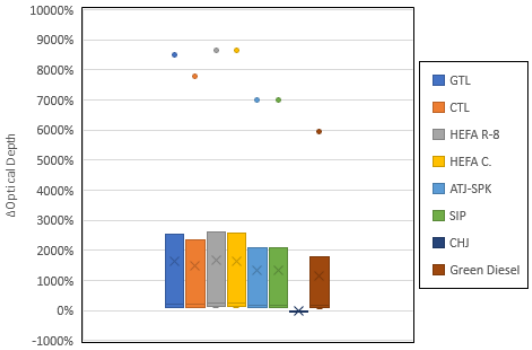

Figure 13: RDs in peak optical depths and initial ice mass ratios for ambient RHs at formation in the range of 40 % to 41 % between SAF and Jet A-1 fuel.

4.5. Radiative Forcing

The climatic impact of a contrail cirrus is controlled by the product of its width by its optical depth. While the optical depth of a contrail is highest for young contrails, this product increases with contrail age, typically reaching maximum values a few hours into a contrail's lifetime. This makes contrail cirrus, which have much higher lifetimes, responsible for the largest climatic impacts [7].

Figure 14 shows the RDs in the product of the contrail width by optical depth for a RH range of 43 % to 58 % at formation; this is the range containing the bulk of the results. While the Interquartile Range (IQR) for these plots is very small, ∼1 %, there are a high amount of outliers for pure SAF. This is due to the influence of the contrail lifetimes; while most contrails formed in these conditions have similar lifetimes, some contrails settle into more humid locations and end up living far longer.

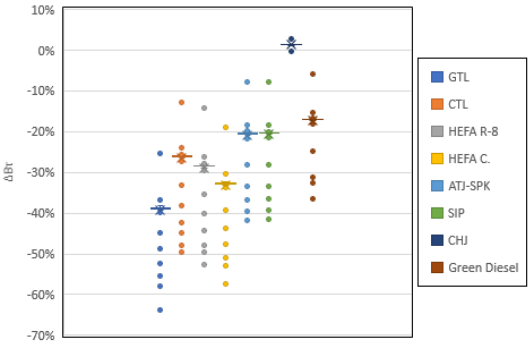

Figure 14: RDs in the product of contrail width by contrail optical depth for ambient RHs at formation of 43 % to 58 % between SAF and Jet A-1 fuel.

Contrails formed at an ambient RH of 58 % or more all lead to long-lasting contrail cirrus. The RDs for the product of width by optical depth is shown in figure 15 separately from the previous range to illustrate their low dispersion.

This range contains contrails with big RDs in peak optical depth values, and absolute differences in lifetime of a few hours. The effect of the contrail age on this product is most clearly felt

here. Since the product of contrail width by optical depth is the factor which controls a contrail's RF, the biggest impact on the climatic influence of contrails when using SAF should be felt for contrail cirrus and not young contrails.

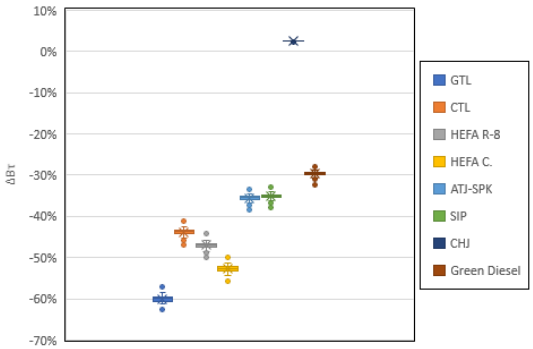

Figure 15: RDs in the product of contrail width by contrail optical depth for ambient RHs at formation of 58 % or higher between SAF and Jet A-1 fuel.

Figure 16 shows the RDs for the contrails formed at a RH of 40 % to 43 %. Below a RH of 40 %, as stated before, all contrails dispersed during the wake vortex phase and thus no calculations are presented.

Contrails formed in this range had peaks at less than one minute of age. Due to this, the peak optical depth and the optical depth at the peak of the product of contrail width by optical depth were very close to each other. Adding to this, the biggest influence on the width of a contrail at these times is the size of the aircraft, which makes the widths between the different fuels also quite similar. This led to a RD trend which was mostly controlled by the peak optical depths.

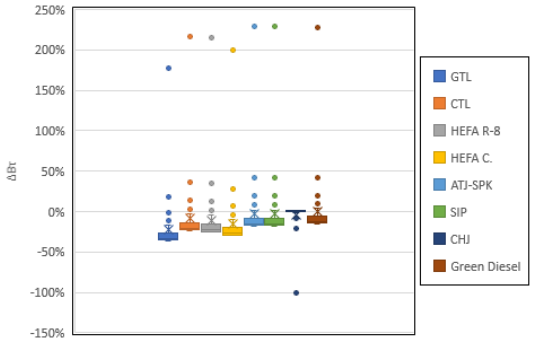

Figure 16: RDs in the product of contrail width by contrail optical depth for ambient RHs at formation of 40 % to 43 % between SAF and Jet A-1 fuel.

5. Conclusions

A contrail-prediction model was implemented with the goal of analysing the effects on contrail properties of burning typical SAF instead of Jet A-1. The contrail model validation showed good agreement, but the auxiliary soot model showed a lacking response to engine power variations, likely as a result of the model not accounting for particle radius variation.

It was found that differences in water vapour emissions between the fuels lead to an increase in contrail formation frequency when very close to reference threshold conditions. Since contrails for SAF form within 1 °C of contrails for Jet A-1, this was translated into longer contrails for SAF and not into isolated SAF contrail segments.

Contrail cirrus had decreases in lifetime when using SAF of up 76 %, with peak MRDs found for pure GTL at –47.94 %. RDs for the lifetime showed a large dispersion, attributed to the heavy dependence this parameter has on local ambient conditions. Nevertheless, a trend of steeper decrease being associated with older Jet A-1 contrails could be seen.

Short-lived contrails had even larger dispersions, with RDs of 800 % found within seconds of RDs of 0 %. Overall they showed slight increases in lifetime, but there were ambient-condition dependent outliers which yielded much larger RDs. While older contrails seem to be influenced more heavily by particle emissions, short-lived contrails seem to be influenced mostly by water vapour emissions.

Peak optical depths were found to be smaller for SAF in most cases, with exceptions being found for contrails formed at a RH range of 40 % to 42 %. Jet A-1 contrails formed in these conditions had peak optical depths with orders of 10^{-4} to 10^{-2}, mostly due to the very low ice water content of the contrails.

The climatic impact of the contrails was measured with the product of contrail width by optical depth, which is the factor which is deemed to control their radiative forcing. As shown by previous studies, the climatic impact of contrail cirrus was found in this work to be much heavier than that of younger contrails.

The product of contrail width by optical depth showed steep decreases for contrail-cirrus formed by SAF, both due to the much smaller lifetimes, and due the big decrease in initial optical depth for these. Younger contrails showed smaller decreases, with contrails formed at a RH of 42 % or lower showing instead an increase in the value of this factor.

Routes in dry locations yielded very short-lived contrails which did not survive past the wake vortex phase. SAF did not influence contrails in this situation, but a more complex large-eddy simulation model could yield different results for this phase. Nevertheless, since the climatic impact of contrails comes largely from them surviving long past the wake vortex phase, the relative importance of any differences found in this phase should be lower.

Routes in more humid locations, such as Europe

and North America, yielded contrails with typically longer lifetimes, which were heavily influenced by the use of SAF. The adoption of SAF and SAF blends in these areas could significantly reduce the climatic impact of both persistent contrails and contrail cirrus.

References

[1] Richard H. Moore, Kenneth L. Thornhill, Bernadett Weinzierl, Daniel Sauer, Eugenio D'Ascoli, Jin Kim, Michael Lichtenstern, Monika Scheibe, Brian Beaton, Andreas J. Beyersdorf, John Barrick, Dan Bulzan, Chelsea A. Corr, Ewan Crosbie, Tina Jurkat, Robert Martin, Dean Riddick, Michael Shook, Gregory Slover, Christiane Voigt, Robert White, Edward Winstead, Richard Yasky, Luke D. Ziemba, Anthony Brown, Hans Schlager, and Bruce E. Anderson. Biofuel blending reduces particle emissions from aircraft engines at cruise conditions. *Nature*, 543(7645):411–415, 2017.

[2] Ulrike Burkhardt and Bernd Kärcher. Global radiative forcing from contrail cirrus. *Nature Climate Change*, 1(1):54–58, 2011.

[3] Lisa Bock and Ulrike Burkhardt. Contrail cirrus radiative forcing for future air traffic. *Atmospheric Chemistry and Physics*, 19:8163–8174, 06 2019.

[4] Klaus Gierens, Peter Spichtinger, and Ulrich Schumann. *Ice Supersaturation*, pages 135–150. Springer Berlin Heidelberg, Berlin, Heidelberg, 2012.

[5] Ulrich Schumann. *Research Topics in Aerospace*. Springer, 2002.

[6] Ulrich Schumann. On conditions for contrail formation from aircraft exhausts. *Meteorologische Zeitschrift*, 5(1):4–23, 03 1996.

[7] U. Schumann. A contrail cirrus prediction model. *Geoscientific Model Development*, 5(3):543–580, 2012.

[8] Hans Hersbach, Carole Peubey, Adrian Simmons, Paul Berrisford, Paul Poli, and Dick Dee. ERA-20CM: A twentieth-century atmospheric model ensemble. *Quarterly Journal of the Royal Meteorological Society*, 141(691):2350–2375, 2015.

[9] R. M. P. Gaspar and J. M. M. Sousa. Impact of alternative fuels on the operational and environmental performance of a small turbofan engine. *Energy Conversion and Management*, 130:81–90, 2016.

[10] N. K. Rizk and H. C. Mongia. Emissions predictions of different gas turbine combustors. *AIAA 94-0118*, 1994.

[11] Ingo Sölch and Bernd Kärcher. A large-eddy model for cirrus clouds with explicit aerosol and ice microphysics and Lagrangian ice particle tracking. *Quarterly Journal of the Royal Meteorological Society*, 136(653):2074–2093, 2010.

[12] J. Um, G. M. McFarquhar, Y. P. Hong, S. S. Lee, C. H. Jung, R. P. Lawson, and Q. Mo. Dimensions and aspect ratios of natural ice crystals. *Atmospheric Chemistry and Physics*, 15(7):3933–3956, 2015.

[13] Raju R. Kumal, Jiawei Liu, Akshay Gharpure, Randy L. Vander Wal, John S. Kinsey, Bob Giannelli, Jeffrey Stevens, Cullen Leggett, Robert Howard, Mary Forde, Alla Zelenyuk, Kaitlyn Suski, Greg Payne, Julien Manin, William Bachalo, Richard Frazee, Timothy B. Onasch, Andrew Freedman, David B. Kittelson, and Jacob J. Swanson. Impact of Biofuel Blends on Black Carbon Emissions from a Gas Turbine Engine. *Energy and Fuels*, 34(4):4958–4966, 2020.

[14] Ulrich Schumann. Formation, properties and climatic effects of contrails. *Comptes Rendus Physique*, 6(4):549 – 565, 2005.

[15] Ulrich Schumann, Philipp Jeßberger, and Christiane Voigt. Contrail ice particles in aircraft wakes and their climatic importance. *Geophysical Research Letters*, 40(11):2867–2872, 2013.

[16] U.S. Environmental Protection Agency. *Determination of Effects of Ambient Conditions on Aircraft Emissions*. 1977.

[17] S C A Kluiters, W P J Visser, and E R Rademaker. A new combustor and emission model for the gas turbine simulation program GSP. 2014.